CHEMISTRY OF MATERIALS

Open Access

pubs.acs.org/cm

Article

First-Principles Statistical Mechanics Study of Magnetic Fluctuations and Order−Disorder in the Spinel $LiNi_{0.5}Mn_{1.5}O_4$ Cathode

Graciela E. García Ponte, Sesha Sai Behara, Euan N. Bassey, Raphaële J. Clément,* and Anton Van der Ven*

Cite This: *Chem. Mater.* 2025, 37, 1835−1846

Read Online

ACCESS | Metrics & More | Article Recommendations | Supporting Information

ABSTRACT: While significant magnetic interactions exist in lithium transition metal oxides, commonly used as Li-ion cathodes, the interplay between magnetic couplings, disorder, and redox processes remains poorly understood. In this work, we focus on the high-voltage spinel $LiNi_{0.5}Mn_{1.5}O_4$ (LNMO) cathode as a model system on which to apply a computational framework that uses first principles-based statistical mechanics methods to predict the finite temperature magnetic properties of materials and provide insights into the complex interplay between magnetic and chemical degrees of freedom. Density functional theory calculations on multiple distinct Ni−Mn orderings within the LNMO system, including the ordered ground-state structure (space group $P4_332$), reveal a preference for a ferrimagnetic arrangement of the Ni and Mn sublattices due to strong antiferromagnetic superexchange interactions between neighboring Mn^{4+} and Ni^{2+} ions and ferromagnetic Mn−Mn and Ni−Ni couplings, as revealed by magnetic cluster expansions. These results are consistent with qualitative predictions using the Goodenough-Kanamori-Anderson rules. Simulations of the finite temperature magnetic properties of LNMO are conducted using Metropolis Monte Carlo. We find that a "semiclassical" Monte Carlo sampling method based on the Heisenberg Hamiltonian accurately predicts experimental magnetic transition temperatures observed in magnetometry measurements. This study highlights the importance of a robust computational toolkit that accurately captures the complex chemomagnetic interactions and predicts finite temperature magnetic behavior to help analyze experimental magnetic and magnetic resonance spectroscopy data acquired *ex situ* and *operando*.

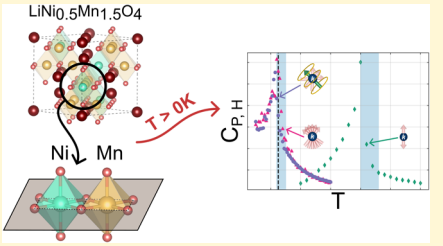

1. INTRODUCTION

Li-ion batteries (LIBs) have become an indispensable component of modern life, enabling the operation of electric and hybrid electric vehicles, as well as portable electronic devices, and the storage of spatially- and temporally dependent renewable energy.[1−4] However, commercial Li-ion battery (LIB) devices suffer from low energy densities and rate capabilities, the cathode material being the performance bottleneck and warranting particular attention for future developments.[4−9]

While most studies of Li-ion battery cathodes still rely on long-range or average characterization tools to monitor the structural rearrangements and redox processes taking place on charge and discharge, the local structure and short-range interactions not only play a key role in their function, but also in their degradation mechanisms.[10−14] In particular, state-of-the-art lithium transition metal (*TM*) oxide cathodes comprise open-shell Ni, Mn, and Co species coupled through strong magnetic exchange and superexchange interactions, and the interplay between these magnetic interactions and redox processes remains to be fully understood. In this regard, magnetic resonance and magnetism-based methods, including nuclear magnetic resonance (NMR),[10,15−18] electron paramagnetic resonance (EPR),[19−21] and magnetometry,[11,19,22−24] stand out as important tools to interrogate the (local) chemical and magnetic structures of these materials.

While recent advances in hardware development have enabled the use of *operando* magnetic and magnetic resonance methods (*i.e.*, those properties are measured during normal battery operation), for *TM*-containing cathode materials, the complexity of the experimental results makes data interpretation challenging.[19,25−27] This is partially due to the large number of local environments coexisting in these complex, multicomponent solids. Additionally, the high concentration of open-shell *TM* species results in significant spectral broadening in NMR and EPR, as well as cooperative magnetic phenomena that are challenging to deconvolute.

Accordingly, the development of computational frameworks to predict the properties of battery cathode materials—particularly their magnetic properties at operational temperatures—is needed to better understand the links between local structure, magnetic couplings, and redox processes, and to

Received: October 3, 2024
Revised: February 13, 2025
Accepted: February 14, 2025
Published: February 25, 2025

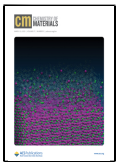

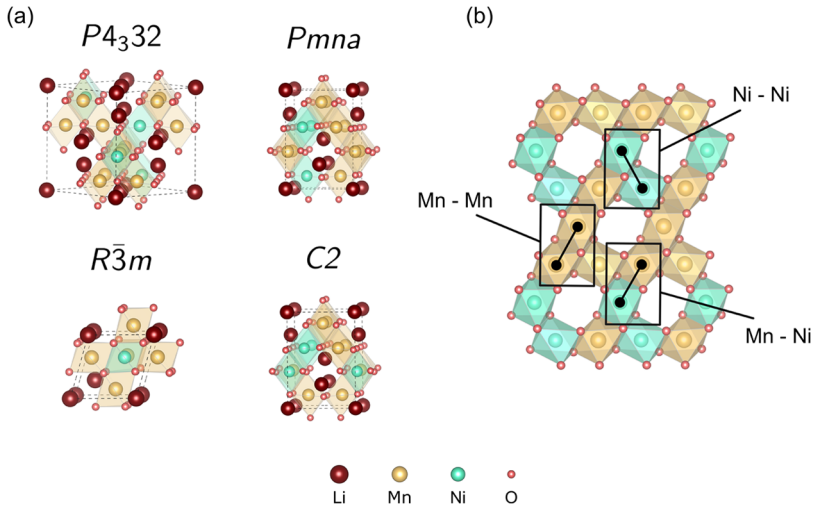

Figure 1. (a) Various crystal structures of the spinel $LiNi_{0.5}Mn_{1.5}O_4$ (LNMO) cathode. The ordered $P4_332$ ground state is shown on the top left, followed by the lower symmetry structures belonging to space groups *Pmna*, $R\bar{3}m$, and *C*2. Figure S1 provides further details between the different chemical orderings on the *TM* planes of the different structures. (b) First nearest neighbor pair interactions used to fit the LNMO spin cluster expansions.

assist data interpretation. In particular, we seek to build a framework in which the magnetic properties of a system may be modeled with respect to spin and chemical occupancy degrees of freedom, so that the influence of each degree of freedom on experimentally observable quantities can be decoupled and connected with battery performance. In this work, we utilize first-principles statistical mechanics methods using cluster expansions and Monte Carlo simulations, as they are an effective way to accurately model finite temperature properties while accounting for chemical disorder, as well as magnetic disorder that might arise from thermal fluctuations[28−35]

Within this context, we focus on the spinel $LiNi_{0.5}Mn_{1.5}O_4$ (LNMO) cathode as a model system for a first-principles statistical mechanics study of finite temperature magnetic properties in cathode materials. LNMO is a high voltage, high capacity cathode[36−39] with a well studied crystal structure. The different types of magnetically active *TM* cations make it possible to investigate the interplay between chemistry and magnetism, as LNMO comprises Mn^{4+} and electrochemically active Ni^{2+} species, both of which are open-shell. Furthermore, the presence of Ni^{2+} makes LNMO a more attractive model than the compositionally simpler $LiMn_2O_4$ (LMO) spinel compound, as it eliminates Jahn−Teller active Mn^{3+} species, which cause local structural distortions and require additional degrees of freedom to model accurately.[36,38,40−44] Finally, the high symmetry of the spinel structure, and nature of the Ni and Mn cations, allow us to neglect spin−orbit-coupling (SOC) interactions, which can nevertheless be treated with the approach used here when significant.[45−47]

Our first-principles density functional theory (DFT) calculations applied to LNMO consistently predict a preference for a ferrimagnetic arrangement of the Ni and Mn sublattices, regardless of their chemical ordering, due to the strong antiferromagnetic superexchange interactions between the Mn^{4+} and Ni^{2+} ions, and the ferromagnetic Mn^{4+}−Mn^{4+} and Ni^{2+}−Ni^{2+} couplings. Spin cluster expansions,[30] which are a generalization of the Heisenberg Hamiltonian, confirm these findings, revealing strong antiferromagnetic Ni−Mn coupling constants and ferromagnetic Mn−Mn and Ni−Ni interactions when trained to the energies of an extensive set of DFT calculations.

We find that Heisenberg statistics are essential to obtain a quantitative agreement between predicted and experimentally measured ferrimagnetic-to-paramagnetic transition temperatures for LNMO. Furthermore, we find that the degree of chemical ordering among Ni and Mn has a negligible effect on the magnetic transition temperature. These predictions are confirmed by experimental measurements of the magnetic properties of two LNMO samples with different degrees of cation ordering. The methodology implemented herein represents a significant step forward in our understanding of the complex interplay between chemistry, magnetism, and other relevant properties. Importantly, it can be applied to the plethora of materials whose functional properties are affected by interacting magnetic spins, including those considered for spintronic, multiferroic, catalysis and energy storage applications.

2. METHODS

2.1. First-Principles Magnetic Hamiltonian. The magnetic moments of *TM* cations in oxides, such as spinel $LiNi_{0.5}Mn_{1.5}O_4$, tend to be localized. In the classical limit, the magnetic moments are not entangled quantum mechanically. Furthermore, they typically maintain a constant length, with only their orientations changing as the solid fluctuates from one magnetic microstate to the next in thermal equilibrium. The magnetic state of a crystal is then specified by the orientation of the magnetic moment at each site *i*, which can be tracked with a collection of unit vectors, $\vec{s}_i$. Within this approximation, the energy of the crystal can be modeled using a Heisenberg Hamiltonian

$$\mathcal{H} = \sum_{\langle i,j \rangle} J_{i,j} \vec{s}_i \cdot \vec{s}_j \tag{1}$$

where $J_{i,j}$ is a measure of the exchange interaction between the i^{th} and j^{th} *TM* sites. The sign of $J_{i,j}$ indicates whether the magnetic moments at sites *i* and *j* prefer to be parallel (negative $J_{i,j}$) or antiparallel (positive $J_{i,j}$). Note the absence of a negative sign in the Hamiltonian, which differs from how it is commonly expressed in the literature.

The Heisenberg Hamiltonian is a truncation of a more rigorous spin cluster expansion,[30] which accommodates all symmetry allowed magnetic interaction terms including the Dzyaloshinskii-Moriya

https://doi.org/10.1021/acs.chemmater.4c02772
Chem. Mater. 2025, 37, 1835−1846

interaction[48] in low symmetry crystals, and higher order polynomials of the elements of $\vec{s}_i$. When the unit vectors $\vec{s}_i$ are restricted to two discrete directions (*e.g.*, up or down), the above Heisenberg Hamiltonian reduces to an Ising model, which itself is a truncation of an alloy cluster expansion.[28]

The interaction constants, $J_{i,j}$, of the Heisenberg Hamiltonian (or, more generally, the expansion coefficients of the spin cluster expansion) can be trained to the energies of a large number of magnetic orderings as calculated with a first-principles electronic structure method such as density functional theory (DFT).[45,46,49−51] In this work, Heisenberg Hamiltonians were parametrized for four distinct orderings of Ni and Mn over the cation sites of the spinel structure with $P4_332$, *Pmna*, $R\bar{3}m$, and *C*2, symmetries (Figure 1a). The expansion coefficients were fit to DFT-r^{2}SCAN[52] energies of colinear magnetic orderings (54 for $P4_332$, 38 for *Pmna*, 15 for $R\bar{3}m$, and 72 for *C*2). The symmetrically distinct colinear magnetic orderings for each chemical ordering were enumerated with the CASM software package.[32,34,53]

The least-squares method, as implemented in Scikit-learn,[54] was then used to obtain the expansion coefficients of each Heisenberg Hamiltonian. While Hamiltonians with exchange interactions that extend to the third nearest neighbor were considered, only the first-nearest neighbor exchange interactions were found to be significant. For example, the Heisenberg Hamiltonian for the $P4_332$ structure with only nearest neighbor exchange interactions replicates DFT energies with a root-mean-square error of less than 0.9 meV per transition metal. Figure 1b shows all the first-nearest neighbor pair interactions used to parametrize the Heisenberg Hamiltonian for the four crystal structures. Figure S2 provides more details about the parametrized models using different levels of truncation.

All electronic structure calculations to parametrize the Heisenberg Hamiltonians were performed with the Vienna *ab initio* simulation package (VASP)[55−57] using the Projector-Augmented-Wave (PAW) method.[58] The r^{2}SCAN[52] exchange-correlation functional was used, as it proved to be significantly more efficient than SCAN while retaining the same accuracy as SCAN.[59−61] The electronic structure calculations were converged to 10^{-5} eV for energies while the forces on atoms were converged to 0.02 eV Å^{-1}. An automatic *k*-point scheme with an R_k length parameter value of 25 Å and a plane wave energy cutoff of 520 eV were used for all calculations. The PAW pseudopotentials used in the DFT calculations were: Li_sv (valency of 3) for lithium, Mn_pv (valency of 13) for manganese, Ni (valency of 10) for nickel, and O (valency of 6) for oxygen. Gaussian smearing with a smearing width of 0.05 eV was used for all the calculations. All calculations performed were colinear spin polarized with magnetic moments on the *TM* species initialized according to the enumerated colinear magnetic orderings.

It is common to model the electronic properties of *TM* oxides using an approximation to density functional theory that is augmented with a Hubbard model correction.[62] The r^{2}SCAN method used in this work is generally accepted to be superior to traditional approximations to DFT, such as the local spin density approximation (LSDA) and the generalized gradient approximation (GGA).[52,59,63] Nevertheless, a recent benchmark study[64] suggested that a Hubbard correction is still necessary when applying SCAN and r^{2}SCAN to transition metal oxides. To test this, we recalculated the energies of all the different magnetic orderings considered in the $P4_332$ ordered LNMO structure, using *U* values of 2.5 and 2.7 eV for Ni and Mn, respectively, as recommended by Gautam and Carter.[65]

These energies were also used to parametrize a Heisenberg Hamiltonian, which was in turn subjected to Heisenberg Monte Carlo simulations. We found that the Heisenberg Hamiltonian parametrized with r^{2}SCAN predicts a magnetic transition temperature that is in better agreement with experimental values than the Heisenberg Hamiltonian parametrized with r^{2}SCAN+*U* calculations, although the difference in predicted transition temperature between the two approaches is less than 50 K. In the results section, we focus primarily on the r^{2}SCAN calculations and summarize the r^{2}SCAN+U calculations in the Supporting Information (Figure S3).

2.2. Statistical Mechanics of Magnetic Degrees of Freedom.

The study of magnetic solids is often performed at constant temperature, *T*, pressure, *P*, and magnetic field, $\vec{H}$. With these thermodynamic boundary conditions, the partition function of statistical mechanics takes the form

$$Z = \sum_{\eta} e^{-\beta\Omega_\eta} \tag{2}$$

where η labels the eigenstates of the quantum mechanical Hamiltonian of the crystal, $\beta = 1/k_BT$ (k_B is Boltzmann's constant) and $\Omega_\eta = E_\eta + PV_\eta - \vec{H}\vec{M}_\eta$ is the generalized enthalpy of the solid for the imposed boundary conditions. In the expression of the generalized enthalpy, E_η is the energy, V_η is the volume and $\vec{M}_\eta$ is the magnetic moment of the solid, all for a given eigenstate η. A magnetic solid in equilibrium fluctuates between different microstates and the probability that the solid resides in microstate ζ at any moment in time is then

$$P_\zeta = \frac{e^{-\beta\Omega_\zeta}}{Z} \tag{3}$$

In the classical limit, each microstate is characterized by a particular orientation of the expectation values of the local magnetic moments. The energy, E_ζ, of a microstate, ζ, can then be modeled with the classical Heisenberg Hamiltonian, eq 1.

The characteristic free energy, Φ, at constant *T*, *P*, and $\vec{H}$, is obtained upon the application of three Legendre transforms to the internal energy, *U*, according to

$$\Phi = U - TS + PV - \vec{H}\vec{M} \tag{4}$$

where *S* is the thermodynamic entropy, *V* is the equilibrium volume and $\vec{M}$ is the equilibrium magnetic moment of the solid. The characteristic free energy is related to the partition function according to

$$\Phi = -k_BT \ln Z \tag{5}$$

This relationship makes it possible to connect thermodynamic state variables and response functions to statistical mechanical averages and variances of fluctuating observables.[66] For example, upon inspection of the differential of Φ (obtained by combining the first and second laws of thermodynamics with the differential of eq 4)

$$d\Phi = -SdT + VdP - \vec{M}d\vec{H} \tag{6}$$

it can be inferred that the magnetic moment of the solid is equal to the partial derivative of Φ with respect to $\vec{H}$ according to

$$\vec{M} = -\left(\frac{\partial\Phi}{\partial\vec{H}}\right)_{P,T} = \frac{\sum_\eta \vec{M}_\eta e^{-\beta\Omega_\eta}}{Z} \tag{7}$$

The second equality in the above relation is obtained using eqs 2 and 5, and shows that the thermodynamic magnetic moment is equal to the statistical mechanical average of the magnetic moments of each microstate.

In a similar way, it is possible to derive expressions for thermodynamic response functions such as the heat capacity, $C_{P,H}$, and magnetic susceptibility, χ.[66] These are related to second derivatives of the characteristic potential and can be calculated as variances of energy and the components of the magnetic moment according to

$$C_{P,H} = \frac{\langle\Omega^2\rangle - \langle\Omega\rangle^2}{Nk_BT^2} \tag{8}$$

$$\chi_{\gamma,\delta} = \frac{\langle M_\gamma M_\delta\rangle - \langle M_\gamma\rangle\langle M_\delta\rangle}{Nk_BT} \tag{9}$$

In these expressions, *N* is the number of magnetic sites in the solid. The subscripts γ and δ in eq 9 refer to Cartesian components of the magnetic moment of the solid along the *x*, *y*, and *z* axes. The

https://doi.org/10.1021/acs.chemmater.4c02772
Chem. Mater. 2025, 37, 1835−1846

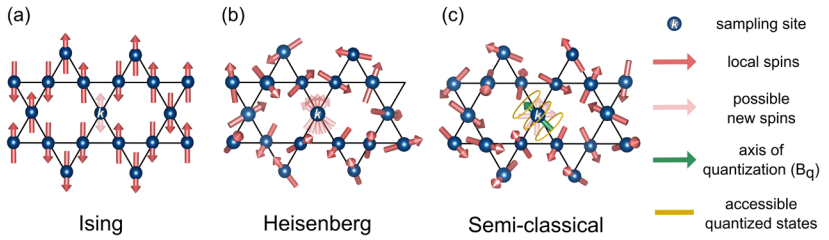

Figure 2. Three Monte Carlo (MC) models used in this study: (a) Ising (IMC), (b) Heisenberg (HMC), and (c) Semiclassical (SCMC). The models are illustrated for the Kagome lattice formed by the *TM* cations in alternating (111) planes of the cubic spinel structure.

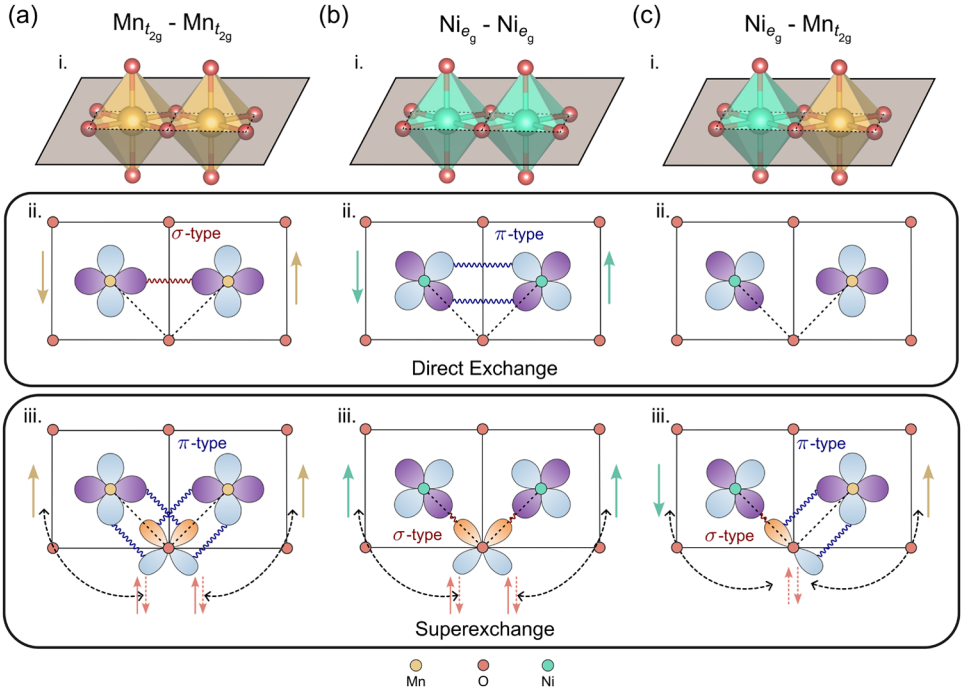

Figure 3. Possible orbital interactions between (a) Mn t_{2g}–Mn t_{2g}, (b) Ni e_g–Ni e_g, and (c) Ni e_g–Mn t_{tg} nearest neighbor transition metal (*TM*) orbitals in LNMO. (a)i, (b)i, and (c)i show Mn–Mn, Ni–Ni, and Ni–Mn octahedra as they appear in the spinel crystal structure. (a)ii, (b)ii, and (c)ii show the possible direct exchange interactions between nearest neighbor *TM* orbital pairs. (a)iii, (b)iii, and (c)iii illustrate the 90° superexchange interactions that can occur between nearest neighbor *TM* orbital pairs via an intermediary oxygen atom. The electrons are colored according to the species they originate from. The σ- and π- type interactions are differentiated with red and blue squiggley lines, respectively.

susceptibility is therefore a second rank tensor that can be represented as a 3 × 3 matrix.

2.3. Monte Carlo Simulations. Thermodynamic averages of state variables (*e.g.*, eq 7) and response functions (*e.g.*, eqs 8 and 9) can be calculated using Monte Carlo simulations, which sample magnetic microstates according to the probability distribution of statistical mechanics, eq 3. We used the Metropolis-Hastings algorithm to sample magnetic microstates at different temperatures and magnetic fields.

Three distinct types of Monte Carlo simulations were performed.[33,34,67] The first uses Ising statistics, where the sampled magnetic moments are only allowed to adopt orientations that are either parallel or antiparallel to the imposed magnetic field (Figure 2a). The second set uses Heisenberg statistics, where the magnetic moments are allowed to adopt any orientation in space by sampling points on a unit sphere (Figure 2b). The third set of Monte Carlo simulations uses a semiclassical Monte Carlo (SCMC) sampling algorithm introduced by Walsh et al.[33] that accounts for the quantized nature of local magnetic moments, as shown in Figure 2c.

While still neglecting quantum mechanical entanglement between neighboring magnetic moments, the SCMC method samples discrete values of the projection of the magnetic moment along a quantization axis determined by the applied magnetic field ($\vec{H}$) and the local field created by neighboring magnetic moments ($\vec{B}_k$). Overall, the field that determines the quantization axis has the form

$$\vec{B}_q = \vec{B}_k - \vec{H} \tag{10}$$

where

$$\vec{B}_k = \sum_{j \neq k} J_{k,j} \vec{s}_j \tag{11}$$

The SCMC algorithm has been found to be more accurate than the classical Heisenberg sampling approach at low temperatures, especially below the magnetic transition temperature.[33]

All Monte Carlo simulations were performed with the CASM software package.[34] Monte Carlo simulations were performed on a fine grid of temperatures between 50 to 600 K in increments of 2–10 K in supercells containing between 3500 and 16,000 magnetic sites. Each site hosting a magnetic moment is visited on average once during a Monte Carlo pass. A total of 10,000 Monte Carlo passes were performed during Ising Monte Carlo (IMC) simulations, of which the first 3000 were excluded before collecting data to perform averages. A total of 20,000 MC passes were performed during both Heisenberg Monte Carlo (HMC) and semiclassical Monte Carlo (SCMC) simulations, with the first 5000 being discarded to allow the system to equilibrate. Average thermodynamic properties such as

https://doi.org/10.1021/acs.chemmater.4c02772
Chem. Mater. 2025, 37, 1835–1846

energy, heat capacity, magnetization, and susceptibility were collected at each temperature using the relations of Section 2.2. Identical exchange interaction coefficients (defined in Section 2.1) were used in the IMC, HMC and SCMC simulations.

While the Heisenberg Hamiltonians used in this work are expressed in terms of unit vectors, $\vec{s}_i$, which track the orientation of the magnetic moment at each site i, the length of the magnetic moment is needed to calculate the Zeeman coupling with the magnetic field and to calculate the total magnetic moment of the crystal. In our study of the LNMO spinel, each local magnetic moment is calculated by multiplying the unit vector $\vec{s}_i$ with $g_e\mu_B\sqrt{s(s+1)}$, where g_e is the electron g-factor, μ_B is the Bohr magneton, and s is the total spin quantum number of the chemical species (*i.e.*, $s_{Mn} = \frac{3}{2}$ and $s_{Ni} = 1$).

2.4. Materials Synthesis. Stoichiometric quantities of NiO, Mn_2O_3 and a 3 mol % excess of Li_2CO_3 were mixed and the resulting powder was pressed into a pellet and calcinated at 500 °C (5 °C/min) for 5 h, then to 850 °C (5 °C/min) for 8 h, and afterward cooled naturally to room temperature. The pellet was then ground. Half of the resulting powder was set aside for further analysis of a more disordered version of LNMO for comparison, while the other half was repelletized and fired at 600 °C (5 °C/min) for 72 h to obtain a more ordered version of LNMO.[20,38,68−71]

2.5. Magnetometry. Magnetic measurements were carried out on a Quantum Design Magnetic Property Measurement System (MPMS3) superconducting quantum interference device (SQUID) magnetometer. Zero field cooled measurements were conducted on LNMO powder samples (∼10−20 mg) over a temperature range from 50 to 300 K and at a magnetic field of 0.1 T. We note that while SQUID measurements are experimentally typically thought of as magnetic susceptibility measurements, in this study, the raw data is not divided by the field and is thus considered as a magnetization measurement.

2.6. X-ray Diffraction. X-ray diffraction patterns of both ordered and disordered LNMO were acquired using a PANAlytical Empyrean diffractometer (Cu Kα radiation, λ = 1.541 Å). Diffraction patterns were acquired over the range 2θ = 5−90° (step size = 0.02°, scanning speed = 0.02° s^{-1}). All Rietveld refinements and XRD data analyses were performed using the TOPAS Academic 7 structure refinement software package.[72]

3. RESULTS

3.1. Goodenough-Kanamori-Anderson Rules for Magnetic Couplings. Goodenough, Kanamori, and Anderson developed and formalized a set of rules (the Goodenough-Kanamori-Anderson (GKA) rules) to qualitatively predict the sign and magnitude of magnetic couplings in transition metal oxide insulators, on the basis of the symmetry, occupancy, and overlap of the interacting and intervening *TM* and O orbitals.[73−75] These rules are used here to rationalize the types of magnetic interactions present in LNMO.

In the spinel LNMO structure, Ni^{2+} and Mn^{4+} species are octahedrally coordinated by oxygen. The electronic configuration of octahedral Mn^{4+} is high spin d^3, with three electrons having parallel spins occupying the t_{2g} orbitals. The octahedral Ni^{2+} cations have a low spin d^8 configuration, with six electrons filling the t_{2g} orbitals and two electrons with parallel spins occupying the e_g orbitals. Hence, the magnetic d orbitals (containing unpaired electrons) are the t_{2g} orbitals of Mn^{4+} and the e_g orbitals of Ni^{2+}.

The $(Ni/Mn)O_6$ octahedra share edges with each other, as shown in Figure 3a(i), b(i), c(i). This arrangement of interstitial *TM*s in the close-packed oxygen framework of spinel allows for direct overlap of their d orbitals, as illustrated in Figure 3a(ii), b(ii), c(ii). Direct overlap of the d orbitals on neighboring Mn sites leads to a σ-type Mn−Mn interaction (Figure 3a(ii)), while for neighboring Ni sites, a Ni−Ni interaction with π character emerges (Figure 3b(ii)). In both cases, direct orbital overlap leads to spin−pairing—*i.e.*, an antiferromagnetic arrangement of neighboring magnetic moments. As the e_g and t_{2g} orbitals on neighboring Ni and Mn species are orthogonal, there is no net overlap between those orbitals, and therefore direct coupling between the Ni and Mn centers is not possible (Figure 3c(ii)).

In addition to direct overlap, the transition metal centers may also interact via an intermediary atom or ion, here oxygen. This is known as superexchange.[73−75] The two relevant interaction limits correspond to *TM*−O−*TM* angles of 180 or 90°. In the LNMO spinel structure, all *TM*−O−*TM* interaction angles are close to 90°, as shown in Figure 3a(iii), b(iii), c(iii). For a Ni−Mn interaction, a single O p orbital is involved in σ−type bonding with the Ni e_g orbital and in π−type bonding with the Mn t_{2g} orbital (Figure 3c(iii)). Since the coupling occurs through a single p orbital, this p orbital must share spins of opposite sign with the two *TM*s (to obey Pauli's principle), leading to a strong antiferromagnetic (AFM) superexchange interaction. Superexchange interactions between the Ni and Mn cations involving empty Mn e_g and half-filled Ni $e_g$or half-filled Mn t_{2g} and full Ni t_{2g} orbitals are expected to be quite weak when compared to the mechanism described above.[74]

For a Mn−Mn or Ni−Ni interaction, a single p orbital is no longer sufficient to enable coupling across the three ions, as its symmetry precludes net orbital overlap with the two magnetic d orbitals on the nearest-neighbor *TM*s. Instead, these superexchange interactions require a second p orbital on the same oxygen (Figure 3a(iii), b(iii)). Since the spins in the two orthogonal O p orbitals obey Hund's third rule and align parallel to one another, *i.e.*, the p orbitals become polarized, leading to sharing of the same spin type with the two nearest-neighbor *TM*s and a weak ferromagnetic (FM) superexchange interaction.

3.2. Magnetic Interactions in $P4_332$ $LiNi_{0.5}Mn_{1.5}O_4$. Having established the expected magnetic couplings between Ni^{2+} and Mn^{4+} nearest neighbors from the GKA rules, we now examine the magnetic couplings derived from first-principles calculations on relevant structural models of LNMO. While the most commonly synthesized form of spinel LNMO has a disordered *TM* sublattice, the ground state adopts an ordered Ni−Mn arrangement as shown in Figure 1a (space group $P4_332$). This $P4_332$ Ni−Mn ordering has the periodicity of the nonprimitive cubic unit cell of the spinel crystal structure, which contains 16 *TM* sites.

Figure 4a shows the DFT energies of 54 symmetrically distinct magnetic configurations in the $P4_332$ structure. The horizontal axis of Figure 4a indicates the fraction of "up" (↑) versus "down" (↓) magnetic moments on the Mn sublattice, while the color of each point measures the fraction of ↑ versus ↓ magnetic moments on the Ni sublattice. The magnetic ground state comprises a ferromagnetic Ni sublattice, and a ferromagnetic Mn sublattice, with the two sublattices aligned antiparallel to one another —*i.e.*, a ferrimagnetic ground state. The high energy states are those in which most of the Ni and Mn magnetic moments are aligned parallel to each other, with the ferromagnetic state (where all Mn and Ni are aligned) having the highest energy.

The DFT energies of the 54 distinct colinear magnetic orderings of $P4_332$ LNMO (Figure 4a) were used to fit the exchange coefficients of a classical Heisenberg Hamiltonian model as described in Section 2.1. While interactions up to the

https://doi.org/10.1021/acs.chemmater.4c02772
Chem. Mater. 2025, 37, 1835−1846

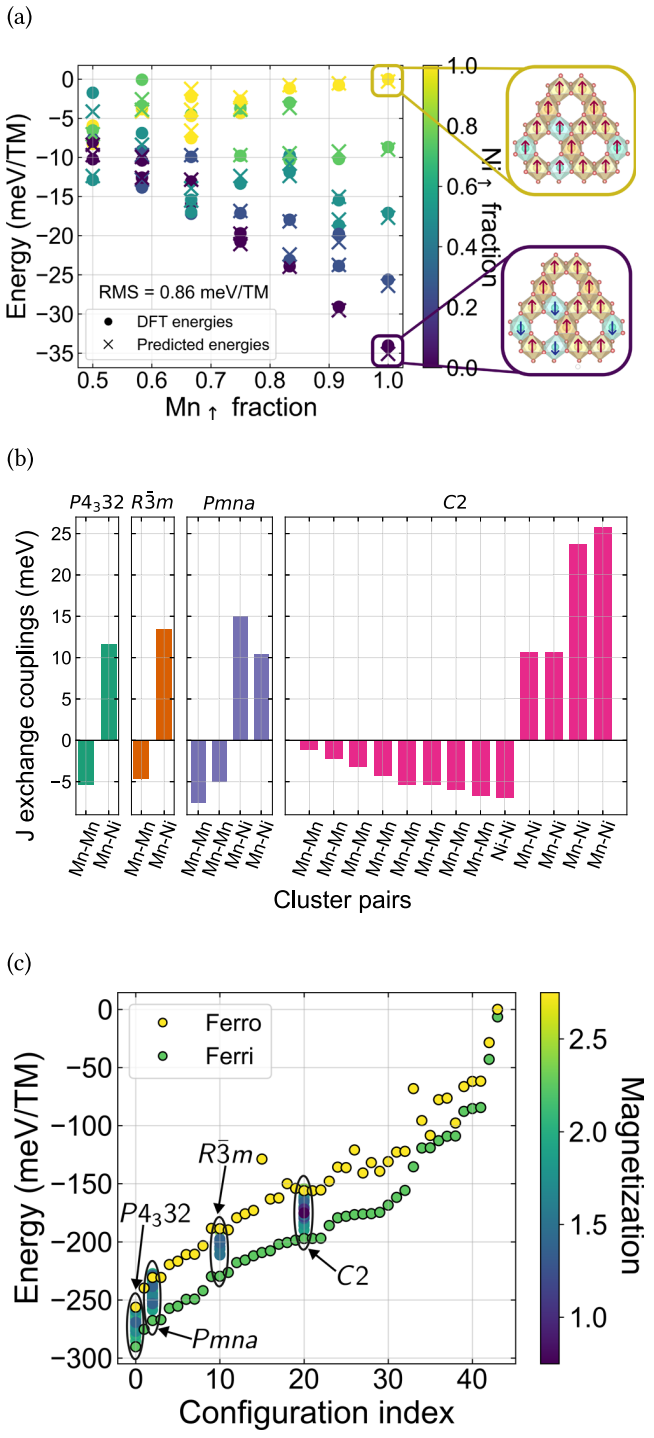

Figure 4. (a) DFT and cluster expansion predicted energies for 54 unique magnetic configurations of $P4_332$ LNMO. $Mn_{\uparrow}$ ($Ni_{\uparrow}$) fractions are defined as the number of Mn ↑ (Ni ↑) spins over the total number of Mn (Ni) spins. (b) First nearest neighbor J exchange couplings of the various LNMO structures obtained from cluster expansion fits. Note that the J values reported in this plot comprise the product of the magnetic moments of the cations in the pair interaction. (c) Energies of various magnetic orderings for several unique Ni−Mn chemical orderings in the LNMO system. The magnetization (M) of each of the orderings is indicated in the figure and is defined according to $M = \frac{2xNi_{\uparrow} + 3yMn_{\uparrow}}{z}$, where x, y, and z are the number of Ni, Mn, and TM ions in each unit cell, respectively.

third nearest neighbor were considered, a root−mean−square (RMS) error of only 0.9 meV/TM was obtained when only first-nearest neighbor pairs were included. The fit is excellent, as is evident upon comparing the DFT energies (circles) to the predictions of the parametrized Heisenberg model (crosses) in Figure 4a.

The expansion coefficients can be interpreted as a measure of pairwise exchange couplings, J. The magnitude of J measures the strength of the magnetic exchange interaction, while its sign defines whether it is ferromagnetic (negative J) or antiferromagnetic (positive J). Note that the Heisenberg Hamiltonian used in this work, which is a truncation of the spin cluster expansion,[30,45] treats the magnetic moments as vectors having unit length and the values reported here for J should be divided by the product of the magnetic moments of the cations of the pair cluster when comparing to exchange terms of commonly used Heisenberg models that are expressed in terms of actual magnetic moments.

As expected from the GKA rules, the Ni−Mn interaction is strongly antiferromagnetic, while the Mn−Mn interaction is somewhat weaker and ferromagnetic as shown in Figure 4b. For the interaction between Ni and Mn, only one magnetic interaction is allowed according to the GKA rules due to the geometry of the orbitals: superexchange mediated through an O p orbital that results in an antiferromagnetic arrangement (Figure 3c(iii)). This result is in agreement with previous *ab initio* work by Lee et al.[76] and Xin et al.,[77] which also predicted a Ni−Mn antiferromagnetic interaction.

For Mn−Mn couplings, the geometry of orbital overlap allows for two competing magnetic interactions between the t_{2g} orbitals: direct exchange, which favors an antiferromagnetic alignment (Figure 3a(ii)), and superexchange, which favors a ferromagnetic arrangement (Figure 3a(iii)). The negative J coefficient obtained by fitting to DFT energies indicates that the latter dominates, most likely because direct orbital overlap is too weak.

3.3. Magnetic Interactions as a Function of Chemical Ordering in $LiNi_{0.5}Mn_{1.5}O_4$. Three additional orderings of Ni and Mn over the TM sites of spinel $LiNi_{0.5}Mn_{1.5}O_4$ were studied in depth to shed light on the dependence of the magnetic ordering on cation (dis)order. The symmetry of the three orderings considered here can be described by the space groups $R\bar{3}m$, *Pmna*, and *C*2, respectively (Figure 1a). The DFT energies of a large number of magnetic orderings in the three structures are shown in Figure 4c.

As in the $P4_332$ structure, the magnetic ground states of the $R\bar{3}m$, *Pmna*, and *C*2 structures are ferrimagnetic, with the Ni magnetic moments parallel to each other but antiparallel to the Mn magnetic moments. Furthermore, the ferromagnetic configuration has the highest energy for the $P4_332$ and $R\bar{3}m$ structures, and is one of the highest energy magnetic orderings for the *Pmna* and *C*2 structures. Figure 4c shows that the spread in energy when varying the magnetic ordering for a fixed Ni−Mn arrangement is significantly smaller than the energy range spanned when varying the Ni−Mn ordering for a fixed magnetic ordering. For example, the energy difference between the ferrimagnetic ground state and the ferromagnetic state in the $P4_332$ structure is less than 40 meV/TM, while the energy difference between the $P4_332$ and *C*2 structures in their ferrimagnetic ground states is close 90 meV/TM.

Also shown in Figure 4c are the energies of the ferrimagnetic and ferromagnetic configurations for 40 symmetrically distinct Ni−Mn orderings over the TM sites of LNMO. Based on the

https://doi.org/10.1021/acs.chemmater.4c02772
Chem. Mater. 2025, 37, 1835−1846

analysis of the $P4_332$, $R\bar{3}m$, *Pmna*, and *C*2 structures, these two magnetic states tend to bracket the energy range spanned by all possible magnetic orderings for a fixed chemical ordering. The spread in energy between the ferromagnetic and ferrimagnetic states is consistently less than 50 meV/*TM*, while the energy of different chemical orderings for the same magnetic state spans a range of almost 300 meV/*TM*. These results suggest that chemical disorder, well-known to exist in LNMO, is expected to preserve ferrimagnetic ordering. Furthermore, they also suggest that less thermal energy is required to induce a magnetic transition than an order−disorder transition among the *TM* cations, although a full statistical mechanics treatment that couples chemical and magnetic disorder would be necessary to quantify this.[49]

The DFT calculation results for the 40+ symmetrically distinct Ni−Mn orderings also reveal a direct correlation between the energy of a particular chemical ordering (irrespective of the magnetic ordering) and the number of Ni−Ni nearest neighbor pairs, as shown in Figure S4. The energy of the structure generally increases with the number of Ni−Ni nearest neighbor pairs, implying that it is energetically unfavorable for Ni ions to cluster together.

Nearest-neighbor Heisenberg Hamiltonians were parametrized for the $R\bar{3}m$, *Pmna*, and *C*2 structures by performing least-squares fits to the energies of different magnetic orderings in each structure. Due to the lower symmetries of the $R\bar{3}m$, *Pmna*, and *C*2 structures, there are more symmetrically unique nearest-neighbor pairs with a distinct exchange coefficient *J*. The first nearest-neighbor exchange coefficients for the three structures are compared to those of $P4_332$ in Figure 4b. Similar trends are exhibited across the four structures for the Ni−Mn and Mn−Mn pairs, with negative (ferromagnetic) *J* values for Mn−Mn interactions and larger, positive (antiferromagnetic) *J* values for Ni−Mn interactions. In contrast to the other structures, the particular Ni−Mn ordering of the *C*2 structure has Ni−Ni nearest neighbors. The exchange coupling, *J*, for the Ni−Ni pairs is negative (ferromagnetic), suggesting a stronger ferromagnetic superexchange delocalization mechanism (Figure 3b(iii)) compared to the competing direct exchange mechanism (Figure 3b(ii)).

3.4. Finite Temperature Magnetic Properties. Monte Carlo simulations were performed using the Heisenberg Hamiltonians for the $P4_332$, $R\bar{3}m$, *Pmna*, and *C*2 spinel structures to study magnetic ordering tendencies as a function of temperature and chemical ordering of LNMO. Three types of Monte Carlo simulations were performed, each differing in the microstates that were sampled: Ising Monte Carlo (IMC) (Figure 2a), Heisenberg Monte Carlo (HMC) (Figure 2b), and a semiclassical Monte Carlo (SCMC) (Figure 2c) algorithm recently introduced by Walsh et al.[33] (See Methods Section 2.3)

Figure 5a compares the calculated heat capacities of the $P4_332$ structure as calculated with the IMC, HMC and SCMC simulations. The heat capacities in Figure 5a are due to magnetic excitations and neglect contributions from vibrational excitations, which are not considered in this study. The calculated heat capacities all exhibit a divergence that is suggestive of a second-order phase transition. This divergence occurs at 450 K when using IMC, but at 120 K when using the HMC and SCMC sampling methods. Above the transition, LNMO is a paramagnet characterized by the absence of long-range order among the magnetic moments. Below the transition, it is ferrimagnetic, with the magnetic moments on the Mn sublattice aligned antiparallel to those on the Ni sublattice.

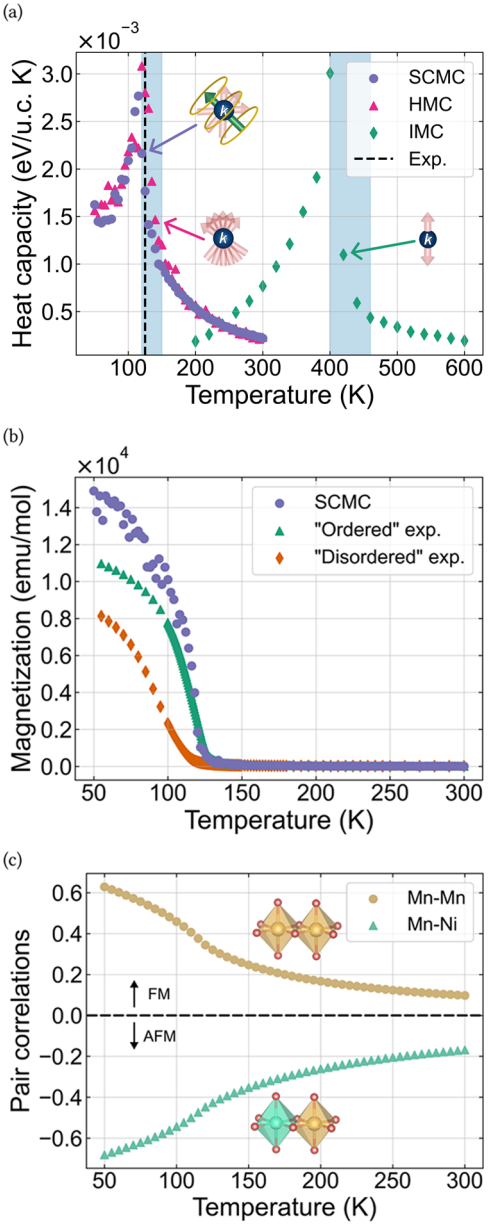

Figure 5. (a) Heat capacity as a function of temperature for the $P4_332$ structure as predicted by IMC, HMC, and SCMC models at zero field. The black dashed line indicates the experimental transition temperature. The shaded blue regions indicate the span of transition temperatures for the other structures. (b) SQUID (magnetization) measurements at 0.1 T as a function of temperature for the experimentally synthesized structures plotted along with field-oriented magnetization data from SCMC, also calculated at 0.1 T. (c) Average pair correlations (dot products) between first-nearest neighbor pairs as a function of temperature. Positive values indicate some degree of FM alignment, while negative values describe some AFM alignment.

The heat capacities of the *Pmna*, $R\bar{3}m$, and *C*2 structures were also calculated with IMC and HMC simulations. The transition temperatures for these structures (estimated to be the temperatures at which the heat capacity diverges) all fall within the light blue shaded regions in Figure 5a. When using IMC, the transition temperatures of the lower-symmetry structures range between 400−460 K, while for HMC, they

https://doi.org/10.1021/acs.chemmater.4c02772
Chem. Mater. 2025, 37, 1835−1846

span a range between 120−150 K. The effect of chemical ordering on the magnetic transition temperature is not significant. For the three long-range ordered structures, the predicted temperatures are larger than that of the $P4_332$ ground state structure.

The large difference in the predicted transition temperatures between the IMC and the HMC and SCMC sampling methods can be attributed to large differences in the entropy of the paramagnetic state. Since the Ising model only allows for binary magnetic degrees of freedom, its disordered state has significantly fewer microstates than those sampled with the HMC and SCMC approaches, where the magnetic moments can adopt significantly more orientations in three-dimensional space.

Figure 5b shows the temperature dependence of the magnetization as calculated with the SCMC algorithm, along with the experimentally measured magnetization for two spinel LNMO samples (green and orange points), all at a magnetic field of 0.1 T. The two samples correspond to a more ordered version of LNMO (green points), and a more disordered version (orange points), as indicated by the Rietveld refinements of laboratory X-ray diffraction data shown in Figure S5. As expected, the magnetization is zero in the paramagnetic region and increases continuously as the low-temperature ferrimagnetic ordering emerges below the magnetic transition temperature. The transition temperature inferred from the computed heat capacity, magnetization, and magnetic susceptibility (Figure S6) using SCMC simulations is close to the experimentally measured transition temperature of ∼130 K for the partially ordered sample. Our measured transition temperature is also consistent with previous reports.[78,79]

Interestingly, while $P4_332$ LNMO no longer exhibits long-range magnetic order in the paramagnetic regime, some degree of short-range ordering between the Mn and Ni magnetic moments persists well above the transition temperature, as indicated by the finite pair correlations (which track the average dot product between pair interactions in the Monte Carlo simulations) in Figure 5c. In particular, the antiferromagnetic short-range ordering of the Ni and Mn magnetic moments (as manifested by a negative pair correlation) remains appreciable even at room temperature.

Overall, the results presented here suggest that the use of HMC or SCMC methods is essential to accurately describe magnetic excitations in spinel LNMO, and that the limited degrees of freedom in the Ising model are too restrictive to enable an accurate thermodynamic description of the paramagnetic phase. Furthermore, the good agreement between experimental and predicted transition temperatures suggests that the classical Heisenberg Hamiltonian is an accurate energy model for the magnetic excitations in spinel LNMO.

While the HMC approach is able to accurately predict the experimental transition temperature, it does not properly model spin behavior at low temperatures due to the quantum nature of spins. In contrast, the SCMC algorithm[33] incorporates the quantum nature of the magnetic moments when sampling magnetic microstates (See the Methods Section 2.3 and Figure 2c). In the SCMC sampling algorithm, the magnetic moment vectors are quantized along the direction of the local magnetic field (eq 10), with $2s+1$ discrete values (s is the total spin), but have continuous degrees of freedom in the plane perpendicular to the magnetic field.[33] This difference leads to slight deviations between the predicted thermodynamic properties as calculated with the Heisenberg and SCMC approaches below the magnetic transition temperature (Figure S7).

In the Heisenberg Monte Carlo simulations, the Ni and Mn magnetic moments are perfectly antialigned when LNMO adopts its ferrimagnetic ground state at low temperatures. In the SCMC simulations, the components of the magnetic moments of Ni and Mn parallel to the local magnetic field are quantized. Therefore, they are unable to adopt a fully antiparallel alignment due to quantum fluctuations. We note that the SCMC algorithm is not a fully quantum mechanical approach as it neglects quantum entanglement between neighboring magnetic moments, but it does account for the quantization of local magnetic moments in a local effective magnetic field created by neighboring spins and the applied field. The effect of the quantum fluctuations can be observed in Figure S7, where the energy predicted with SCMC sampling is slightly higher than that of classical HMC simulations.

4. DISCUSSION

Magnetic interactions can play an important role in determining the electronic, electrochemical, thermodynamic, and kinetic properties of transition metal oxides commonly used for catalysis and in battery devices.[22,23,45,46,61] Furthermore, the magnetic properties of a particular compound can reveal much about its electronic and structural properties. The ability to accurately predict magnetic properties of a system from first-principles implies that a fundamental understanding of the relevant quantum mechanical interactions and finite temperature magnetic excitations has been established.

In this work, we performed an in-depth study of the magnetic properties of spinel $LiNi_{0.5}Mn_{1.5}O_4$ (LNMO), using a first-principles statistical mechanics approach and validating our predictions with experimental measurements. The comparison between predicted and measured magnetic properties allowed us to assess the accuracy of the underlying quantum mechanical description of the magnetic interactions and identify the optimal sampling of statistical mechanical excitations in the Monte Carlo simulations. The predicted magnetization and magnetic transition temperature using the Heisenberg Monte Carlo (HMC) and semiclassical Monte Carlo (SCMC)[33] approaches are in very good agreement with experimental values. This implies that the classical Heisenberg Hamiltonian, parametrized using the energies of different magnetic orderings as calculated with DFT-r^{2}SCAN, is an accurate model of the magnetic interactions in LNMO.

In using a classical Heisenberg Hamiltonian to model the energy of the system, correlations are neglected between neighboring magnetic moments that are quantum mechanically entangled. Such correlations are only expected to be significant at temperatures that are well below the magnetic transition temperature of LNMO, which ranges between 120 and 150 °C depending on the degree of (dis)order on the *TM* sublattice. The large discrepancy between the experimental transition temperature and that predicted using the Ising Monte Carlo (IMC) approach indicates that a two-state representation of the spins is too restrictive to accurately describe magnetic disorder within the paramagnet. The degrees of freedom available to each magnetic moment in the Heisenberg Monte Carlo and SCMC approaches, in contrast, are substantially larger than those available to an Ising magnet, leading to a significantly more stable paramagnetic phase.[80]

https://doi.org/10.1021/acs.chemmater.4c02772
Chem. Mater. 2025, 37, 1835−1846

The magnetic interactions between the Ni^{2+} and Mn^{4+} cations in the spinel host structure, as extracted from extensive DFT-r^{2}SCAN calculations, are consistent with the Goodenough-Kanamori-Anderson (GKA) rules. An antiferromagnetic interaction is predicted between nearest neighbor Ni^{2+} and Mn^{4+}, which can be attributed to a strong delocalization-type superexchange interaction between the Ni and the Mn ions involving an intervening oxygen ion. This antiferromagnetic interaction between nearest neighbor Ni−Mn pairs is predicted for all four ordered configurations of Ni and Mn in LNMO considered in this work. A ferromagnetic interaction within Mn−Mn pairs (and Ni−Ni pairs in the case of the *C*2 structure) is predicted and can be explained via a weaker polarization-type superexchange interaction. As a result of these interactions, the ground state magnetic ordering in LNMO is independent of the Ni/Mn ordering and ferrimagnetic, with the Ni magnetic moments aligned antiparallel to the Mn magnetic moments. The interactions, though, are not particularly strong as manifested by the low magnetic transition temperatures.

Interestingly, the Heisenberg and SCMC simulations predict that short-range ordering (antialignment) of the Ni^{2+} and Mn^{4+} magnetic moments persists up to room temperature. These findings suggest that the common understanding of paramagnets as comprising fully random spin orientations with magnetic pair correlations equal to zero is erroneous. The predicted short-range ordering likely has subtle and nuanced implications not only for magnetometry, but also for the interpretation of electrochemical, NMR and EPR measurements.[10,11,13,14] We expect that the antiferromagnetic superexchange interaction between Ni^{2+} and Mn^{4+} is present in other transition metal oxides such as the layered $Li_x(Ni_{1-y-z}Mn_yCo_z)O_2$ (NMC) intercalation compounds, which are actively studied for use in commercial Li-ion batteries.

The study presented here is restricted to the fully lithiated form of the LNMO spinel compound, but additional insights can be gained upon extending this methodology to model magnetism as a function of charge. Doing so, however, presents a number of new challenges. When Li is extracted from LNMO, Ni^{2+} oxidizes first to Ni^{3+} and finally to Ni^{4+} at the end of charge.[38,39] These different redox states on the Ni will affect the dominant GKA interactions, and therefore change the magnetic properties of the lowest energy states. Furthermore, Ni^{3+} is Jahn−Teller active, which will cause local distortions of the NiO_6 octahedra within the spinel structure. These distortions may interact with Li vacancies and lead to some degree of short-range ordering between the Ni^{3+} cations and Li vacancies. Exploring these interactions will provide insight into the coupling between magnetic and electrochemical properties in cathode materials. However, this will require more complex cluster expansion Hamiltonians[32,34] that include magnetic,[30] chemical,[28,29,49] displacement[44,81−84] and charge/orbital[43,85] ordering degrees of freedom and will be the focus of future work.

5. CONCLUSIONS

Modeling the magnetic properties of battery materials is not only important for the interpretation of experimental data, but also to develop a fundamental understanding of the nature of magnetism and its relationship with the electrochemistry of the material. In this paper, we investigated the magnetic ordering tendencies of $LiNi_{0.5}Mn_{1.5}O_4$ for different Ni−Mn orderings. We found that the magnetic interactions in LNMO are consistent with the Goodenough-Kanamori-Anderson rules, with a ferrimagnetic arrangement between the magnetic moments of the Ni and Mn sublattices being favored energetically. Furthermore, the delocalization achieved via superexchange consistently dominates over the direct exchange mechanism in Mn−Mn and Ni−Ni interactions. We found that Monte Carlo simulations based on Heisenberg and semiclassical Monte Carlo microstate sampling algorithms are significantly more accurate than Ising model statistics in predicting magnetic transition temperatures. The excellent agreement between predicted magnetic transition temperatures and experimentally measured temperatures suggests that a classical Heisenberg model Hamiltonian, trained to r^{2}SCAN DFT calculations, is an accurate model to describe magnetic interactions in LNMO at finite temperatures. Furthermore, our results reveal a residual antiferromagnetic short-range ordering present between the transition metal pairs even after the paramagnetic transition.

■ ASSOCIATED CONTENT

Supporting Information

The Supporting Information is available free of charge at https://pubs.acs.org/doi/10.1021/acs.chemmater.4c02772.

Crystal structures of spinel LNMO based on various possible Ni−Mn ordering on the transition metal (*TM*) lattice; Magnetic (*J*) exchange couplings for the $P4_332$ LNMO structure obtained from three different cluster expansion fits; Analysis of energies with different Hubbard (U) parameters; Energies of ferromagnetic and ferrimagnetic orderings for various Ni−Mn orderings as a function of Ni−Ni pair correlations; Rietveld refinements of "ordered" $P4_332$ and "disordered" $Fd\bar{3}m$ LNMO samples; Magnetization, heat capacity, and magnetic susceptibility of $P4_332$ as obtained through SCMC simulations; Energy landscapes for the $P4_332$ structure as a function of temperature as calculated from Heisenberg and SCMC Monte Carlo simulations (PDF)

■ AUTHOR INFORMATION

Corresponding Authors

Raphaële J. Clément − *Materials Department, University of California Santa Barbara, Santa Barbara, California 93106, United States; Materials Research Laboratory, University of California Santa Barbara, Santa Barbara, California 93106, United States*; Email: rclement@ucsb.edu

Anton Van der Ven − *Materials Department, University of California Santa Barbara, Santa Barbara, California 93106, United States*; Email: avdv@ucsb.edu

Authors

Graciela E. García Ponte − *Materials Department, University of California Santa Barbara, Santa Barbara, California 93106, United States*

Sesha Sai Behara − *Materials Department, University of California Santa Barbara, Santa Barbara, California 93106, United States*; orcid.org/0000-0003-2144-4586

Euan N. Bassey − *Materials Department, University of California Santa Barbara, Santa Barbara, California 93106, United States; Materials Research Laboratory, University of California Santa Barbara, Santa Barbara, California 93106, United States*; orcid.org/0000-0001-8827-7175

https://doi.org/10.1021/acs.chemmater.4c02772
Chem. Mater. 2025, 37, 1835−1846

Complete contact information is available at:
https://pubs.acs.org/10.1021/acs.chemmater.4c02772

Notes

The authors declare no competing financial interest.

■ ACKNOWLEDGMENTS

G.E.G.P. acknowledges Alen Maguire for his assistance in the synthesis of the LNMO material. G.E.G.P. also acknowledges funding from UCSB under her Chancellor's Fellowship. This work was supported by the Office of Naval Research (ONR), Award No. N00014-23-1-2333. Use was made of computational facilities purchased with funds from the National Science Foundation (CNS-1725797) and administered by the Center for Scientific Computing (CSC). The CSC is supported by the California NanoSystems Institute and the Materials Research Science and Engineering Center (MRSEC; NSF DMR 2308708) at UC Santa Barbara. The research reported here made use of the shared facilities of the Materials Research Science and Engineering Center (MRSEC) at UC Santa Barbara: NSF DMR-2308708. The UC Santa Barbara MRSEC is a member of the Materials Research Facilities Network (www.mrfn.org). We are also grateful for the resources of the National Energy Research Scientific Computing Center (NERSC), a U.S. Department of Energy Office of Science User Facility located at Lawrence Berkeley National Laboratory, operated under Contract No. DE-AC02-05CH11231 using NERSC award BES-ERCAP0026626. Research was also carried out at the Center for Functional Nanomaterials, Brookhaven National Laboratory, through the U.S. Department of Energy, Office of Basic Energy Sciences, contract DE-AC02-98CH10866, under award CFN312109.

■ REFERENCES

(1) Li, W.; Erickson, E. M.; Manthiram, A. High-nickel layered oxide cathodes for lithium-based automotive batteries. *Nat. Energy* **2020**, *5*, 26−34.
(2) Schmuch, R.; Wagner, R.; Hörpel, G.; Placke, T.; Winter, M. Performance and cost of materials for lithium-based rechargeable automotive batteries. *Nat. energy* **2018**, *3*, 267−278.
(3) Andre, D.; Kim, S.-J.; Lamp, P.; Lux, S. F.; Maglia, F.; Paschos, O.; Stiaszny, B. Future generations of cathode materials: an automotive industry perspective. *J. Mater. Chem. A* **2015**, *3*, 6709−6732.
(4) Myung, S.-T.; Maglia, F.; Park, K.-J.; Yoon, C. S.; Lamp, P.; Kim, S.-J.; Sun, Y.-K. Nickel-rich layered cathode materials for automotive lithium-ion batteries: achievements and perspectives. *ACS Energy Lett.* **2017**, *2*, 196−223.
(5) Goodenough, J. B.; Kim, Y. Challenges for rechargeable Li batteries. *Chem. Mater.* **2010**, *22*, 587−603.
(6) Chu, S.; Majumdar, A. Opportunities and challenges for a sustainable energy future. *Nature* **2012**, *488*, 294−303.
(7) Whittingham, M. S. Lithium batteries and cathode materials. *Chem. Rev.* **2004**, *104*, 4271−4302.
(8) Radin, M. D.; Hy, S.; Sina, M.; Fang, C.; Liu, H.; Vinckeviciute, J.; Zhang, M.; Whittingham, M. S.; Meng, Y. S.; Van der Ven, A. Narrowing the gap between theoretical and practical capacities in Li-ion layered oxide cathode materials. *Adv. Energy Mater.* **2017**, *7*, No. 1602888.
(9) Nitta, N.; Wu, F.; Lee, J. T.; Yushin, G. Li-ion battery materials. *Mater. Today* **2015**, *18*, 252−264.
(10) Märker, K.; Xu, C.; Grey; C P Operando, N. M. R. of NMC811/graphite lithium-ion batteries: structure, dynamics, and lithium metal deposition. *J. Am. Chem. Soc.* **2020**, *142*, 17447−17456.
(11) Bassey, E. N.; Seymour, I. D.; Bocarsly, J. D.; Keen, D. A.; Pintacuda, G.; Grey, C. P. Superstructure and Correlated Na+ Hopping in a Layered Mg-Substituted Sodium Manganate Battery Cathode are Driven by Local Electroneutrality. *Chem. Mater.* **2023**, *35*, 10564−10583.
(12) Bassey, E. N.; Reeves, P. J.; Jones, M. A.; Lee, J.; Seymour, I. D.; Cibin, G.; Grey, C. P. Structural origins of voltage hysteresis in the Na-ion cathode P2-Na0. 67 [Mg0. 28Mn0. 72] O2: a combined spectroscopic and density functional theory study. *Chem. Mater.* **2021**, *33*, 4890−4906.
(13) Seymour, I. D.; Chakraborty, S.; Middlemiss, D. S.; Wales, D. J.; Grey, C. P. Mapping structural changes in electrode materials: application of the hybrid eigenvector-following density functional theory (DFT) method to layered Li0. 5MnO2. *Chem. Mater.* **2015**, *27*, 5550−5561.
(14) Haworth, A. R.; Cook, C. W.; Griffin, J. M. Solid-state NMR studies of coatings and interfaces in batteries. *Interface Sci.* **2022**, *62*, No. 101638.
(15) Grey, C. P.; Dupré, N. NMR studies of cathode materials for lithium-ion rechargeable batteries. *Chem. Rev.* **2004**, *104*, 4493−4512.
(16) Carlier, D.; Ménétrier, M.; Grey, C.; Delmas, C.; Ceder, G. Understanding the NMR shifts in paramagnetic transition metal oxides using density functional theory calculations. *Phys. Rev. B* **2003**, *67*, No. 174103.
(17) Grenier, A.; Reeves, P. J.; Liu, H.; Seymour, I. D.; Märker, K.; Wiaderek, K. M.; Chupas, P. J.; Grey, C. P.; Chapman, K. W. Intrinsic kinetic limitations in substituted lithium-layered transition-metal oxide electrodes. *J. Am. Chem. Soc.* **2020**, *142*, 7001−7011.
(18) Pecher, O.; Carretero-González, J.; Griffith, K. J.; Grey, C. P. Materials' methods: NMR in battery research. *Chem. Mater.* **2017**, *29*, 213−242.
(19) Nguyen, H.; Clément, R. J. Rechargeable batteries from the perspective of the electron spin. *ACS Energy Lett.* **2020**, *5*, 3848−3859.
(20) Niemöller, A.; Jakes, P.; Eurich, S.; Paulus, A.; Kungl, H.; Eichel, R.-A.; Granwehr, J. Monitoring local redox processes in LiNi0. 5Mn1. 5O4 battery cathode material by in operando EPR spectroscopy. *J. Chem. Phys.* **2018**, *148*, No. 014705.
(21) Stoyanova, R.; Gorova, M.; Zhecheva, E. EPR monitoring of Mn4+ distribution in Li4Mn5O12 spinels. *J. Phys. Chem. Solids* **2000**, *61*, 615−620.
(22) Mukherjee, P.; Paddison, J. A.; Xu, C.; Ruff, Z.; Wildes, A. R.; Keen, D. A.; Smith, R. I.; Grey, C. P.; Dutton, S. E. Sample Dependence of Magnetism in the Next-Generation Cathode Material LiNi0. 8Mn0. 1Co0. 1O2. *Inorg. Chem.* **2021**, *60*, 263−271.
(23) Li, Q.; Li, H.; Xia, Q.; Hu, Z.; Zhu, Y.; Yan, S.; Ge, C.; Zhang, Q.; Wang, X.; Shang, X.; et al. Extra storage capacity in transition metal oxide lithium-ion batteries revealed by in situ magnetometry. *Nat. Mater.* **2021**, *20*, 76−83.
(24) Biecher, Y.; Baux, A.; Fauth, F.; Delmas, C.; Goward, G. R.; Carlier, D. Structure and Electronic Structure Evolution of P2-Na x CoO2 Phases from X-ray Diffraction and 23Na Magic Angle Spinning Nuclear Magnetic Resonance. *Chem. Mater.* **2022**, *34*, 6431−6439.
(25) Nguyen, H.; Bassey, E.; Foley, E.; Kitchaev, D.; Giovine, R.; Clément, R. Operando electron spin probes for the study of battery processes. *J. Magn. Reson.* **2024**, *368*, No. 107772.
(26) Niemöller, A.; Jakes, P.; Eichel, R.-A.; Granwehr, J. In operando EPR investigation of redox mechanisms in LiCoO2. *Chem. Phys. Lett.* **2019**, *716*, 231−236.
(27) Tang, M.; Dalzini, A.; Li, X.; Feng, X.; Chien, P.-H.; Song, L.; Hu, Y.-Y. Operando EPR for simultaneous monitoring of anionic and cationic redox processes in Li-rich metal oxide cathodes. *J. Phys. Chem. Lett.* **2017**, *8*, 4009−4016.
(28) Sanchez, J. M.; Ducastelle, F.; Gratias, D. Generalized cluster description of multicomponent systems. *Phys. A* **1984**, *128*, 334−350.
(29) De Fontaine, D. *Solid State Physics*; Elsevier, 1994; Vol. *47*, pp 33−176.

(30) Drautz, R.; Fähnle, M. Spin-cluster expansion: Parametrization of the general adiabatic magnetic energy surface with ab initio accuracy. *Phys. Rev. B* **2004**, *69*, No. 104404.
(31) Walle, A.; Ceder, G. Automating first-principles phase diagram calculations. *J. Phase Equilib.* **2002**, *23*, 348.
(32) Van Der Ven, A.; Thomas, J. C.; Puchala, B.; Natarajan, A. R. First-Principles Statistical Mechanics of Multicomponent Crystals. *Annu. Rev. Mater. Res.* **2018**, *48*, 27−55.
(33) Walsh, F.; Asta, M.; Wang, L.-W. Realistic magnetic thermodynamics by local quantization of a semiclassical Heisenberg model. *npj Comput. Mater.* **2022**, *8*, 186.
(34) Puchala, B.; Thomas, J. C.; Van der Ven, A. CASM Monte Carlo: Calculations of the thermodynamic and kinetic properties of complex multicomponent crystals. arXiv:2309.11761. arXiv.org e-Print archive. https://arxiv.org/abs/2309.11761, 2023.
(35) Wang, N.; Hammerschmidt, T.; Rogal, J.; Drautz, R. Accelerating spin-space sampling by auxiliary spin dynamics and temperature-dependent spin-cluster expansion. *Phys. Rev. B* **2019**, *99*, No. 094402.
(36) Liu, G. Q.; Wen, L.; Liu, Y. M. Spinel LiNi 0.5 Mn 1.5 O 4 and its derivatives as cathodes for high-voltage Li-ion batteries. *J. Solid State Electrochem.* **2010**, *14*, 2191−2202.
(37) Wang, L.; Li, H.; Huang, X.; Baudrin, E. A comparative study of Fd-3m and P4332 "liNi 0.5Mn1.5O4. *Solid State Ionics* **2011**, *193*, 32−38.
(38) Kim, J.-H.; Myung, S.-T.; Yoon, C.; Kang, S.; Sun, Y.-K. Comparative study of LiNi0. 5Mn1. 5O4-δ and LiNi0. 5Mn1. 5O4 cathodes having two crystallographic structures: fd$\bar{3}$m and P 4332. *Chem. Mater.* **2004**, *16*, 906−914.
(39) Manthiram, A.; Chemelewski, K.; Lee, E.-S. A perspective on the high-voltage LiMn 1.5 Ni 0.5 O 4 spinel cathode for lithium-ion batteries. *Energy Environ. Sci.* **2014**, *7*, 1339−1350.
(40) Shu, J.; Yi, T. F.; Shui, M.; Wang, Y.; Zhu, R. S.; Chu, X. F.; Huang, F.; Xu, D.; Hou, L. Comparison of electronic property and structural stability of LiMn 2O4 and LiNi0.5Mn1.5O4 as cathode materials for lithium-ion batteries. *Comput. Mater. Sci.* **2010**, *50*, 776−779.
(41) Ouyang, C. Y.; Shi, S. Q.; Lei, M. S. Jahn-Teller distortion and electronic structure of LiMn2O4. *J. Alloys Compd.* **2009**, *474*, 370−374.
(42) Verhoeven, V. W.; Mulder, F. M.; De Schepper, I. M. Influence of Mn by Li substitution on the Jahn-Teller distortion in LiMn2O4. *Phys. B* **2000**, *276−278*, 950−951.
(43) Radin, M. D.; Van der Ven, A. Simulating charge, spin, and orbital ordering: application to Jahn-Teller distortions in layered transition-metal oxides. *Chem. Mater.* **2018**, *30*, 607−618.
(44) Radin, M. D.; Thomas, J. C.; Van der Ven, A. Order-disorder versus displacive transitions in Jahn-Teller active layered materials. *Phys. Rev. Mater.* **2020**, *4*, No. 043601.
(45) Kitchaev, D. A.; Schueller, E. C.; Van der Ven, A. Mapping skyrmion stability in uniaxial lacunar spinel magnets from first principles. *Phys. Rev. B* **2020**, *101*, No. 054409.
(46) Kitchaev, D. A.; Van der Ven, A. Tuning magnetic antiskyrmion stability in tetragonal inverse Heusler alloys. *Phys. Rev. Mater.* **2021**, *5*, No. 124408.
(47) Walsh, F.; Natarajan, A. R.; Van der Ven, A. Order parameters for antiferromagnetic structures: A first-principles study of iridium manganese. *Phys. Rev. Mater.* **2022**, *6*, No. 044402.
(48) Dzyaloshinsky, I. A thermodynamic theory of "weak" ferromagnetism of antiferromagnetics. *J. Phys. Chem. Solids* **1958**, *4*, 241−255.
(49) Decolvenaere, E.; Levin, E.; Seshadri, R.; Van der Ven, A. Modeling magnetic evolution and exchange hardening in disordered magnets: The example of Mn 1- x Fe x Ru 2 Sn Heusler alloys. *Phys. Rev. Mater.* **2019**, *3*, No. 104411.
(50) Schueller, E. C.; Kitchaev, D. A.; Zuo, J. L.; Bocarsly, J. D.; Cooley, J. A.; Van der Ven, A.; Wilson, S. D.; Seshadri, R. Structural evolution and skyrmionic phase diagram of the lacunar spinel GaMo 4 Se 8. *Phys. Rev. Mater.* **2020**, *4*, No. 064402.
(51) Zuo, J. L.; Kitchaev, D.; Schueller, E. C.; Bocarsly, J. D.; Seshadri, R.; Van der Ven, A.; Wilson, S. D. Magnetoentropic mapping and computational modeling of cycloids and skyrmions in the lacunar spinels GaV 4 S 8 and GaV 4 Se 8. *Phys. Rev. Mater.* **2021**, *5*, No. 054410.
(52) Furness, J. W.; Kaplan, A. D.; Ning, J.; Perdew, J. P.; Sun, J. Accurate and Numerically Efficient r 2 SCAN Meta-Generalized Gradient Approximation. *J. Phys. Chem. Lett.* **2020**, *11* (19), 8208−8215.
(53) Puchala, B.; Thomas, J. C.; Natarajan, A. R.; Goiri, J. G.; Behara, S. S.; Kaufman, J. L.; Van der Ven, A. CASM − A software package for first-principles based study of multicomponent crystalline solids. *Comput. Mater. Sci.* **2023**, *217*, No. 111897.
(54) Pedregosa, F.; Varoquaux, G.; Gramfort, A.; et al. Scikit-learn: Machine Learning in Python. *J. Mach. Learn. Res.* **2011**, *12*, 2825−2830.
(55) Kresse, G.; Hafner, J. Ab initio molecular dynamics for liquid metals. *Phys. Rev. B* **1993**, *47*, 558−561.
(56) Kresse, G.; Furthmüller, J. Efficiency of ab-initio total energy calculations for metals and semiconductors using a plane-wave basis set. *Comput. Mater. Sci.* **1996**, *6*, 15−50.
(57) Kresse, G.; Furthmü, J. Efficient iterative schemes for ab initio total-energy calculations using a plane-wave basis set. *Phys. Rev. B* **1996**, *54*, No. 11169.
(58) Kresse, G.; Joubert, D. From ultrasoft pseudopotentials to the projector augmented-wave method. *Phys. Rev. B* **1999**, *59*, 1758−1775.
(59) Kingsbury, R.; Gupta, A. S.; Bartel, C. J.; Munro, J. M.; Dwaraknath, S.; Horton, M.; Persson, K. A. Performance comparison of r 2 SCAN and SCAN metaGGA density functionals for solid materials via an automated, high-throughput computational workflow. *Phys. Rev. Mater.* **2022**, *6*, No. 013801.
(60) Yang, J. H.; Kitchaev, D. A.; Ceder, G. Rationalizing accurate structure prediction in the meta-GGA SCAN functional. *Phys. Rev. B* **2019**, *100*, No. 35132.
(61) Kitchaev, D. A.; Vinckeviciute, J.; Van der Ven, A. Delocalized metal-oxygen π-redox is the origin of anomalous nonhysteretic capacity in Li-ion and Na-ion cathode materials. *J. Am. Chem. Soc.* **2021**, *143*, 1908−1916.
(62) Anisimov, V. I.; Zaanen, J.; Andersen, O. K. Band theory and Mott insulators: Hubbard U instead of Stoner I. *Phys. Rev. B* **1991**, *44*, 943.
(63) Sun, J.; Remsing, R. C.; Zhang, Y.; Sun, Z.; Ruzsinszky, A.; Peng, H.; Yang, Z.; Paul, A.; Waghmare, U.; Wu, X.; et al. Accurate first-principles structures and energies of diversely bonded systems from an efficient density functional. *Nat. Chem.* **2016**, *8*, 831−836.
(64) Sai Gautam, G.; Carter, E. A. Evaluating transition metal oxides within DFT-SCAN and SCAN+ U frameworks for solar thermochemical applications. *Phys. Rev. Mater.* **2018**, *2*, No. 095401.
(65) Swathilakshmi, S.; Devi, R.; Sai Gautam, G. Performance of the r2scan functional in transition metal oxides. *J. Chem. Theory Comput.* **2023**, *19*, 4202−4215.
(66) Hill, T. L. *Statistical Mechanics: Principles And Selected Applications*; Courier Corporation, 2013.
(67) Walle, A. v. d.; Asta, M. Self-driven lattice-model Monte Carlo simulations of alloy thermodynamic properties and phase diagrams. *Modell. Simul. Mater. Sci. Eng.* **2002**, *10*, 521.
(68) Idemoto, Y.; Narai, H.; Koura, N. Crystal structure and cathode performance dependence on oxygen content of LiMn1. 5Ni0. 5O4 as a cathode material for secondary lithium batteries. *J. Power Sources* **2003**, *119−121*, 125−129.
(69) Kunduraci, M.; Al-Sharab, J. F.; Amatucci, G. G. High-power nanostructured LiMn2-x Ni x O4 high-voltage lithium-ion battery electrode materials: electrochemical impact of electronic conductivity and morphology. *Chem. Mater.* **2006**, *18*, 3585−3592.
(70) Park, S.; Oh, S.-W.; Kang, S. H.; Belharouak, I.; Amine, K.; Sun, Y.-K. Comparative study of different crystallographic structure of LiNi0. 5Mn1. 5O4- δ cathodes with wide operation voltage (2.0 − 5.0 V). *Electrochim. Acta* **2007**, *52*, 7226−7230.

https://doi.org/10.1021/acs.chemmater.4c02772
Chem. Mater. 2025, 37, 1835−1846

(71) Chong, J.; Xun, S.; Song, X.; Liu, G.; Battaglia, V. S. Surface stabilized LiNi0. 5Mn1. 5O4 cathode materials with high-rate capability and long cycle life for lithium ion batteries. *Nano Energy* **2013**, *2*, 283−293.
(72) Coelho, A. A. TOPAS and TOPAS-Academic: an optimization program integrating computer algebra and crystallographic objects written in C++. *J. Appl. Crystallogr.* **2018**, *51*, 210−218.
(73) Goodenough, J. B. An interpretation of the magnetic properties of the perovskite-type mixed crystals La1- xSrxCoO3- λ. *J. Phys. Chem. Solids* **1958**, *6*, 287−297.
(74) Goodenough, J. B. *Magnetism and the Chemical Bond*; Interscience Publisher: New York, 1663.
(75) Streltsov, S. V.; Khomskii, D. I. Orbital physics in transition metal compounds: new trends. *Phys.-Usp.* **2017**, *187*, 1205−1235.
(76) Lee, E.; Persson, K. A. Revealing the coupled cation interactions behind the electrochemical profile of Li xNi 0.5Mn 1.5O 4. *Energy Environ. Sci.* **2012**, *5*, 6047−6051.
(77) Xin, X. G.; Shen, J. T.; Shi, S. Q. Structural and magnetic properties of LiNi 0.5 Mn 1.5 O 4 and LiNi 0.5 Mn 1.5 O 4 - δ spinels: A first-principles study. *Chin. Phys. B* **2012**, *21*, No. 128202.
(78) Amdouni, N.; Zaghib, K.; Gendron, F.; Mauger, A.; Julien, C. Magnetic properties of LiNi0. 5Mn1. 5O4 spinels prepared by wet chemical methods. *J. Magn. Magn. Mater.* **2007**, *309*, 100−105.
(79) Strobel, P.; Palos, A. I.; Anne, M.; Le Cras, F. Structural, magnetic and lithium insertion properties of spinel-type Li2Mn3MO8 oxides (M= Mg, Co, Ni, Cu). *J. Mater. Chem.* **2000**, *10*, 429−436.
(80) Domb, C.; Sykes, M. Effect of change of spin on the critical properties of the Ising and Heisenberg models. *Phys. Rev.* **1962**, *128*, 168.
(81) Thomas, J. C.; Ven, A. V. d. Finite-temperature properties of strongly anharmonic and mechanically unstable crystal phases from first principles. *Phys. Rev. B* **2013**, *88*, No. 214111.
(82) Thomas, J. C.; Bechtel, J. S.; Natarajan, A. R.; Van der Ven, A. Machine learning the density functional theory potential energy surface for the inorganic halide perovskite CsPbBr 3. *Phys. Rev. B* **2019**, *100*, No. 134101.
(83) Bechtel, J. S.; Thomas, J. C.; Van der Ven, A. Finite-temperature simulation of anharmonicity and octahedral tilting transitions in halide perovskites. *Phys. Rev. Mater.* **2019**, *3*, 113605.
(84) Saber, M.; Behara, S. S.; Van der Ven, A. Redox Mechanisms, Structural Changes, and Electrochemistry of the Wadsley-Roth Li x TiNb2O7 Electrode Material. *Chem. Mater.* **2023**, *35*, 9657−9668.
(85) Zhou, F.; Maxisch, T.; Ceder, G. Configurational Electronic Entropy and the Phase Diagram of Mixed-Valence Oxides: The Case of Li x FePO 4. *Phys. Rev. Lett.* **2006**, *97*, No. 155704.

https://doi.org/10.1021/acs.chemmater.4c02772
Chem. Mater. 2025, 37, 1835−1846